The Distribution of Peak-Ring Basins on Mercury and their Correlation with the High-Mg/Si Terrane

G. P. Hall[1], A. Martindale[1], J. C. Bridges[1], L. R. Nittler[2], and E. J. Bunce[1]

[1]School of Physics and Astronomy, University of Leicester, UK.

[2]Department of Terrestrial Magnetism, Carnegie Institution of Washington, USA.

Corresponding author: Graeme Hall (gph11@le.ac.uk)

Key Points:

- There is a statistically strong spatial correlation between a group of 15 peak-ring basins on Mercury and the high Mg/Si region.

- Crater uplift modelling, and an absence of associated volcanic landforms, suggests excavation of deep crustal material with high Mg/Si.

- The High Mg/Si region will be a key target for MIXS-T on BepiColombo to test the model of deep crustal excavation.

Abstract

A catalogue of mercurian craters that retain their central peak or peak-ring structure was created to aid target prioritisation for the Mercury Imaging X-ray Spectrometer (MIXS), now on its way to Mercury aboard BepiColombo. Preliminary analysis of the MIXS crater catalogue suggested a potential spatial correlation between an abnormally high spatial density of peak-ring basins and a region of Mercury with elevated Mg/Si values (High-Magnesium Terrane, HMT). Robust statistical analysis of previously published crater catalogues confirmed that the spatial correlation exists, with an overall confidence level of 97.7 %, specifically between peak-ring basins and the HMT, delineated by a contour of Mg/Si = mean+2σ = 0.648. Applying empirical impact cratering scaling laws to the 15 basins intersecting the HMT suggested that all have excavated material from ~13–20 km depth. None of the basins excavated mantle material, predicting instead that deep crustal material contains elevated Mg/Si material. However, five of the basins are predicted to have melted underlying mantle material, which might be a contributing factor in the elevated Mg/Si signature. In the absence of resolvable volcanic features associated with the rise of basaltic melts from the mantle, we favour excavation of deep crustal, high Mg/Si material. MIXS-T is capable of spatially resolving individual features associated with peak-ring basins and it is proposed that the 15 basins within the HMT are prioritised targets for MIXS, to test the hypothesis of exposed deep-crustal material.

Plain Language Summary

A catalogue of craters that retain a central peak, or peak-ring, structure, was created in order to prioritise targets for the Mercury Imaging X-ray Spectrometer on the BepiColombo mission. Preliminary analysis of this catalogue revealed a potential spatial correlation between a region with an abnormally high spatial density of peak-ring basins and a region with high Magnesium-to-Silicon ratios. Robust statistical analysis of previously published crater catalogues was used to confirm the spatial correlation exists. Investigation of the depth of excavation for material ejected during impact indicates that the impacts within the main high Mg/Si terrane excavated deep crustal, rather than mantle, material of high Mg/Si ratio. Current X-ray data does not spatially resolve the basin features to confirm these hypotheses but future observations by the Mercury Imaging X-ray Spectrometer are capable of doing so.

1 Introduction

In December 2025, the joint ESA and JAXA BepiColombo mission will enter orbit around Mercury to begin a one-year nominal plus one-year extended science mission (Benkhoff et al., 2010). Among the 16 instruments, shared across 2 spacecraft, is the Mercury Imaging X-ray Spectrometer (MIXS) on board the Mercury Planetary Orbiter (MPO). The MIXS instrument represents the first time a true-imaging X-ray spectrometer has been sent to another planet and it is expected to offer unprecedented insights into the surface elemental composition of Mercury (Bunce et al., 2020; Fraser et al., 2010). This instrument will follow on from the successful MESSENGER mission (Solomon & Anderson, 2018) which has posed a number of questions of great scientific importance for follow up by BepiColombo.

As part of target prioritisation for the MIXS instrument, we identified a need for a catalogue of all craters that retain a central peak (or peak-ring) structure, resolvable by MIXS

(Data Set S1; Tables S1 and S2; Figures S1 to S8). Interestingly, upon completion of the MIXS crater catalogue we identified a potential spatial correlation between an abnormally high spatial density of peak-ring basins (PRB) and the high-magnesium terrane (HMT), a region of Mercury showing high Mg/Si values in the MESSENGER X-Ray Spectrometer (XRS) data set (Weider et al., 2015). To simplify discussion, this abnormally high spatial density will hereafter be referred to as an 'over-density'. In this paper, we report on statistical analyses carried out to confirm the correlation, using other published data sets, and explore whether impact events could offer a plausible mechanism for the elevated Mg/Si values.

1.1 Complex Craters and Basins

Complex craters and basins, which still have the peak structures visible (hereafter referred to as 'peaked' craters), have long been understood to uplift material from deep crustal and upper mantle levels (e.g. Grieve (1987); Melosh (1989); Spudis (1993)). Analysis of lunar craters has demonstrated peak structures are an important target for understanding the composition and evolution of planetary lithospheres (e.g. Moriarty et al. (2013); Song et al. (2013); Tompkins and Pieters (1999)). As ancient crust (4.0 to 4.5 Ga) is expected to be in low abundance on the surface of Mercury (Denevi et al., 2018), impact craters may offer a mechanism for excavating into ancient crust beneath more recent features.

Although work has been carried out to calculate the initial depth of uplifted material (e.g. Cintala and Grieve (1998); Melosh (1989); Potter et al. (2013)), the equations have been derived from lunar or terrestrial craters, so their applicability to Mercury is limited. However, Croft (1985) determined that crater features can be scaled according to the simple-to-complex transition diameter, as this accounts for the effects of gravity and target properties. Further work by Potter and Head (2016) has also indicated that the excavation depths for the Moon and Mercury are roughly comparable, so the equations are considered useful, although the results should be treated with some degree of caution. This is discussed in more detail in Section 2.4.

1.2 The Geochemical Terranes of Mercury

Current knowledge of Mercury's geochemical composition comes from the MErcury Surface, Space ENvironment, Geochemistry and Ranging (MESSENGER) mission (Solomon & Anderson, 2018). The primary geochemical instruments aboard MESSENGER were the X-ray Spectrometer (Schlemm et al., 2007) and the Gamma-ray and Neutron Spectrometer (Goldsten et al., 2007). The MESSENGER mission used a highly elliptical orbit which gave the X-ray Spectrometer (XRS) footprints of ~200 km towards the north pole and ~1800 km towards the south pole. This orbit meant that the data collected by the XRS was of particularly low resolution in the southern hemisphere. Element detection that relied on serendipitous solar-flare states (S, Ca, Ti, Cr, Mn, Fe) was incomplete in the northern hemisphere, however, data for Mg, Al, and Si was obtained for the entire surface, from the upper ~10's of micrometres (Weider et al., 2015). The data were presented as element-to-Si ratios as these are easier to measure, remove some systematic errors, and Si has been observed to vary less across the surface than the other elements (Peplowski et al., 2012). In contrast, data from the Gamma-ray Spectrometer (GRS) and Neutron Spectrometer (NS) were only obtained for latitudes above ~10° N. The GRS was able to detect C, O, Na, Al, Si, K, S, Cl, Ca, Fe, Th, and U, from the upper ~10's of centimetres of the surface. Elements detected by both instruments were shown to be in good agreement with each other (Nittler et al., 2018). The NS is sensitive to bulk compositions and only detected the

individual elements H and C. The results indicate a heterogeneous surface with distinct geochemical terranes. McCoy et al. (2018) identified five different geochemical terranes; Southern Hemisphere, Northern Terrane, Caloris Interior Plains, Low-Fast Terrane, High-Magnesium Terrane (HMT). A detailed description of the different compositions is given in McCoy et al. (2018).

The HMT, which is the focus of this paper, exhibits the highest Mg/Si, S/Si, Ca/Si, and Fe/Si ratios observed on Mercury, as well as low Al/Si ratios. Weider et al. (2015) used a threshold Mg/Si value of 0.5 to define the HMT. It covers an area from approximately 120° W to 45° W and from approximately 10° S to 50° N, with an area $>5\times10^6$ km^2. It has been suggested that the HMT could be an impact basin remnant, due to its low elevation (Weider et al., 2015). However, Frank et al. (2017) conclude that this is unlikely due to a lack of clear structural evidence, beyond relatively low elevation and crustal thickness, and a topographic boundary to the north. Frank et al. (2017) suggest that the modification of a basin structure should also have erased the chemical signature. Thus, they conclude that the HMT was most likely the signature of a heterogeneous underlying mantle and the region is not geologically unique, compared to the rest of Mercury. Another possibility is that basin-size impacts into relatively thin lithosphere caused fracturing, which subsequently allowed the extrusion of mantle-derived basalts through the basin floors. The large footprint of the XRS precluded analysis of individual craters and their features, which may reveal the origin of the HMT. This study investigated a correlation between impact basins and the HMT. More detailed analysis probed the distribution of high-Mg/Si material within the lithosphere of Mercury (Section 3.3).

1.3 The Stratigraphy of Mercury

It is generally accepted that most of Mercury's crust was emplaced by widespread volcanism, during the first billion years, during the pre-Tolstojan and Tolstojan eras (Denevi et al., 2018). Vander Kaaden and McCubbin (2015) proposed that – on the basis of Mercury having an unusually reduced bulk geochemistry – a primary graphite flotation crust may have formed initially, as carbon would have been the most buoyant element in a Mercury magma ocean. This crust would subsequently be incorporated into the ancient crust during magmatic and impact events (Denevi et al., 2018). Regions of low-reflectance material (LRM) have up to 6 wt % carbon (Peplowski et al., 2016) suggesting that if a graphite crust existed, it must have mixed with the ancient silicate crust. The relatively high (~1 wt %) carbon content in the surface of Mercury (Peplowski et al., 2016), and the elevated carbon content of excavated LRM, suggests that the ancient silicate crust was relatively carbon-rich (Klima et al., 2018), whether a graphite primary crust formed or not.

Extensive resurfacing has made evaluating the nature of the ancient crust very difficult, although the signature may have been preserved in a heavily gardened form (Denevi et al., 2018) in the oldest, least volcanically resurfaced regions, identified as the northern and southern heavily cratered terrains (HCT) by Marchi et al. (2013). The northern HCT partially coincides with the western region of the HMT. Marchi et al. (2013) used crater size-frequency distribution methods to determine that the northern HCT formed 4.0–4.1 Gyr ago, at the start of the Late Heavy Bombardment (LHB). The volcanic resurfacing of Mercury at this time would have covered any ancient crust that still remained. However, the northern HCT has undergone the least volcanic resurfacing, so impact gardening may have revealed some of the ancient crust and possibly the upper mantle.

Recent crust (<4.0 Ga) includes contributions from LRM, which simulations have predicted to exist at mid-crustal levels (Rivera-Valentin & Barr, 2014), but is also formed from volcanic eruption of the high-temperature counterparts of iron-poor basalts (e.g. basaltic komatiites), which may have a mantle origin and mixed with ancient crust during ascent (Phillips et al., 2018). Material derived from partial melting of the mantle would generally be higher in reflectance than the ancient crust, as carbon has already been partitioned from the mantle and into the ancient crust. This can be observed in the high-reflectance red plains (e.g. Borealis Planitia), although low-reflectance blue plains (e.g. circum-Caloris) may also be volcanic in origin (Denevi et al., 2018).

The HMT also coincides with the northern part of the Vivaldi region, which is of approximately pre-Tolstojan age. The stratigraphy of this region, proposed by Denevi et al. (2018), is of a thin layer of moderately reflective plains material overlaying a deposit 3–4 km thick of high-reflectance red material (HRM), which in turn overlays a layer of LRM. There are likely vertical and horizontal heterogeneities in the material too. The HRM is believed to be of volcanic origin and pre-Tolstojan in age. Denevi et al. (2018) and Fassett et al. (2012) suggest that the absence of craters >300 km in diameter is evidence of extensive resurfacing. However, Wieczorek et al. (2012) suggest that a period of synchronous orbit can explain the lack of craters >300 km in diameter in specific regions of the surface.

2 Methods

2.1 Defining the High-Mg/Si Terrane

The High-Mg/Si terrane (HMT) of Mercury was initially defined by Weider et al. (2015) as a region centred on ~30° N and 290° E with an area >5×10^6 km^2. However, a precise definition was required for robust statistical analysis. It was determined that the best approach was to use a one-tail hypothesis test to define confidence contours. Nittler et al. (2018) gives the global mean Mg/Si value as $\mu^C = 0.436$ with a standard deviation of $\sigma^C = 0.106$. This gives the null hypothesis, H_0^C, that the Mg/Si value equals the mean value, and the alternative hypothesis, H_1^C, that the Mg/Si value is greater than the mean value:

$$H_0^C : Mg/Si = 0.436; \qquad H_1^C : Mg/Si > 0.436. \qquad (1)$$

Using $\sigma^C = 0.106$, we can determine the confidence contours for the HMR, which are given in Table 1 and shown in Figure 1, mapped over the MESSENGER XRS data (Nittler, 2016). Three high-Mg/Si terranes (HMST) have been defined, referred to hereafter as the 1σ-, 1.5σ- and 2σ-HMST (Table 1). As the focus is on the HMT, only contours between 150° W and 30° W were included in the analysis.

2.2 Crater Catalogues

The crater catalogue created by the authors was for the express purpose of target prioritization for the MIXS instrument. The key premise of the catalogue is that craters must retain a central peak/ring structure, as these have a chance of being resolvable with MIXS-T, given appropriate viewing conditions. This catalogue will be referred to as the 'MIXS' catalogue (Data Set S1). The catalogue is designed to allow prioritization of targets as the optimal observing conditions will be serendipitous. The classification system grades the same features as

other systems but with an emphasis on that which is important for the MIXS target list. Simplicity has been considered by using distinct categories for the features, allowing easy classification, and predominantly using single characters for input. It is assumed that correlation with other systems can be achieved by selecting subgroups of craters that have specific properties, defined by the other systems. The features graded were: crater type, freshness, ejecta, peak type, terracing, floor-wall contact, superposed craters, and infilling. A full description of the classifications is given in Table S1, with examples provided in Figures S2 to S8. It should be noted that the catalogue was created by inspecting imagery from the Mercury MESSENGER MDIS Global Basemap BDR 166 m map (Denevi et al., 2017) not through morphometric measurements. Although the titular 'correlation' was first observed in the MIXS crater catalogue, this cataloguing work was not carried out with the same accuracy as published mercurian crater catalogues. Thus, to ensure rigor, it was necessary to carry out all further analysis using published catalogues.

Baker and Head (2013) catalogued basins with a peak-ring, protobasins, and ring-cluster basins. Protobasins were defined by a central peak and peak ring, and ring-cluster basins defined by a central ring cluster. Ring-cluster basins are transitional from mature complex craters to protobasins. The basins were identified using morphometric techniques and peak-ring basins include those which have wrinkle ridge or scarp formations instead of a visible peak-ring. Baker and Head (2013) updated Baker et al. (2011), adding more peak-ring basins and protobasins, and including all craters with a central peak and diameter ≥50 km. All entries were classified using the C1 (fresh) to C5 (degraded) system, where lunar and mercurian classifications were unified in the paper. The Baker and Head (2013) catalogue contained 862 craters and basins and will hereafter be referred to as the 'Baker and Head catalogue'.

Fassett et al. (2011) catalogued all of the craters on Mercury with diameter ≥20 km, using initial flyby data. The size limit was used as it is believed to indicate the boundary at which secondary craters are no longer included in the data set. This allows the relative ages of terrains to be determined using crater counting techniques. Crater rim positions were catalogued but no classification of the craters was carried out. This catalogue was initially created from flyby data but later updated to include the entire surface. Fassett et al. (2012) then added all certain and probable basins with a diameter >300 km. The combined data set contained 7385 craters and will hereafter be referred to as the 'Fassett catalogue'.

Herrick et al. (2018) catalogued the rim position of craters between 5 km and 10 km diameter, and catalogued rim position and infill data for all craters with diameter ≥10 km. The craters between 10 km and 20 km diameter were added to the Fassett catalogue, then the presence of infill material was determined for all craters, based on the discernibility of the original crater morphology. Features of unfilled craters were then graded. The data was presented as two tables, totalling nearly 32,000 craters.

Kinczyk et al. (2020) classified all craters with diameter ≥40 km, taken from the Fassett Catalogue. The classification system is based on the observed degradation of crater features and is applied uniformly to all craters in the catalogue, regardless of size or morphology.

The Baker and Head catalogue was chosen for the primary analysis reported here as it contains all of the large craters and basins that have a central peak. The comprehensive degradation classifications could also be analysed and have been unified to lunar crater classifications. As the Fassett catalogue provides data on the general distribution of all craters,

not including secondary impacts, it provides a useful baseline for comparing subsets of craters against. This baseline was used to determine if any correlations are unique to peaked craters, dependent on crater diameter, or correlated with the density distribution of all craters. The Herrick et al. (2018) catalogue was not used for distribution analysis, as many of the craters are secondary impacts which distorts the distribution. The Kinczyk et al. (2020) catalogue was not used for analysis as the Baker and Head catalogue was preferred, due to its focus on basins and unification of lunar and mercurian classifications.

2.3 Analysis of the Distribution of Basin Populations

To analyse spatial correlations, statistics needed to be gathered from across Mercury. Simply dividing the crater count by the surface area does not provide any standard deviations to allow a statistical analysis to be carried out. To generate global statistics, 10,000 random sampling points (RP) were selected from across the surface of Mercury. Ten thousand points are considered suitable to generate reliable statistics and provide acceptable computation times. The sample points were required to be spatially balanced to avoid oversampling of the polar regions, which would bias the statistics. The RPs acted as the centres for buffers used to collect the crater count statistics. These buffers were generated by calculating the area of the region of interest (ROI) and then calculating the radius of a circle with the same area as the ROI. This radius was then used as the maximum search buffer distance from the RP. All buffers were calculated using geodesic distances to avoid distance distortion caused by specific map projections. Craters or basins were counted by using a buffered crater count method, such that craters that intersected the search buffer were included (Kneissl et al., 2015). Two scenarios were tested; intersections using only the basin and intersections using a buffer of one basin diameter (buffer diameter equals 3 radii from centre) which roughly encircles the ejecta blanket (Baker & Head, 2015; Kneissl et al., 2015). The structure including ejecta blanket is hereafter referred to as the 'total impact structure' or TIS. These two scenarios were tested so we can investigate how ejecta blankets effect the statistics.

To generate the 10,000 spatially balanced random points, we assume that Mercury is spherical. Generating spatially balanced points on an ellipsoid is somewhat more difficult as the spatial balancing is harder to achieve. Also, another step is required as the generated points then have to be converted into the planetocentric coordinates of the data set. Zuber et al. (2012) report a reduction of 2.26 km ± 0.05 km in the north-pole radius, compared to the equatorial radius of 2439.83 km, and Perry et al. (2013) report a 2.2 km ± 0.1 km reduction in the south-pole radius. The variability reported represents a difference of <0.1 % between equatorial and polar radii, so the assumption of a spherical Mercury is assumed to be justified. The random points were generated in ArcGIS with the function 'spatially balanced random points.' This function generates random points with the probability provided by an 'inclusion raster.' The inclusion raster was generated to ensure that the points are evenly spatially distributed in longitude and latitude. This can be achieved by ensuring that any line of longitude or latitude has the same number of random points per km. For longitude, a uniform distribution of random numbers between -180° and +180° are sufficient as each line of longitude is a great circle. Great circles will have the same circumference, thus random points per km, without any dependence on longitude. For latitude, the number of points must be scaled to ensure the same number of random points per km for any given latitude. This can be achieved by scaling the uniform probability of including a random point, based on the latitude of the point. The circumference of Mercury at the equator, C_M, is related to the radius of Mercury, $R_M = 2439.83$ km, by,

$$C_M = 2\pi R_M \qquad (2)$$

and the circumference at any other latitude, C_θ, is related to the radius of Mercury by,

$$C_\theta = 2\pi R_M \cos\theta = C_M \cos\theta. \qquad (3)$$

So, to ensure the same number of craters per km, the number of points need to be scaled by a factor of $\cos\theta$ at latitude θ. Thus, the normalized inclusion probability density is given by:

$$1 = A \int_{-90}^{90} \cos\theta \, d\theta \qquad (4)$$

where A is the normalization factor. Solving this integral gives $A = 1/2$, so the probability of inclusion at latitude θ is,

$$P_i = \frac{\cos\theta}{2}. \qquad (5)$$

The inclusion raster was generated with 768 rows and 1536 columns, ~0.25° bins. Each column in a row contains the same value, representing the independence of longitude, and the rows were assigned probabilities based on P_i. This inclusion raster was then used with the 'spatially balanced random points' function to generate 10,000 points, evenly distributed on a sphere (Section 3). Statistics were then gathered from buffers centred on these points, which can then be used as global statistics for regional comparisons. It was decided that the focus would be on the 2σ-HMST, as this region has a high confidence of greater-than-mean Mg/Si values, which will greatly improve the overall statistics.

Once the statistics have been collected, another one-tailed hypothesis test can be carried out. Let μ^B be the mean number of basins within the buffer radius and C be the actual number of basins within the specific confidence contour, then we have the null hypothesis, H_0^B, that the number of craters within the buffer is equal to the mean, and the alternative hypothesis, H_1^B, that the number of craters within the buffer is greater than the mean:

$$H_0^B : C = \mu^B, \qquad H_1^B : C > \mu^B, \qquad (6)$$

which can be tested for the different scenarios outlined above.

2.4 Uniqueness of Correlations

If a region with an over-density of PRBs is found in the vicinity of the HMT, then it will also be necessary to determine how well the two regions are spatially correlated. We first produce a map of the number of basins intersecting a buffer, where the buffers are centred on a 0.25° grid to coincide with the Mg/Si map (Weider et al., 2015). A contour can then be traced, which encloses all grid cells with a basin count greater-than-or-equal-to the mean basin count plus two standard deviations, hereafter referred to as the 2σ-PRB region. The centre of the 2σ-HMST and 2σ-PRB regions can then be determined, using the centre-of-mass function in ArcGIS, and the distance between the centres can then be measured. Using the assumption that Mercury is spherical, we can trace a great circle between the centres of the two ROIs and determine the angular separation between them, θ_{CEN}. We can then calculate the probability of the centres being randomly separated by $\leq \theta_{CEN}$, P_θ, by solving the integral,

$$P_\theta = \frac{1}{2} \int_{90-\theta_{CEN}}^{90} \cos\theta \, d\theta. \qquad (7)$$

The other uniqueness condition that needs to be tested is whether similar impacts reveal a similar Mg/Si signature. A similar impact is defined as similar to a specific PRB that intersects the 2σ-HMST region (HMT-PRB). Excavation depth is used as a proxy for impact size, to allow investigation of the depth of origin for impact material. Similar is defined as the depth of excavation for a particular HMT-PRB, $Z_{ex}^{HMT-PRB}$, plus or minus 0.5 km. The impact must also be into similar thickness crust as the HMT-PRB, $t_{CRUST}^{HMT-PRB}$, which is defined as a mean crustal thickness, t_{CRUST}, that lies within one standard deviation of $t_{CRUST}^{HMT-PRB}$. The mean crustal thickness is determined by taking the average value of points on a circle of three basin radii, which lies outside the ejecta blanket (Baker & Head, 2015). The crustal thickness data from Genova et al. (2019) is used for this analysis. Genova et al. (2019) computed this data using the HgM008 gravity field and Mercury Laser Altimeter topography data. The crustal thickness was calculated using the assumption that the mean crustal thickness is 35 km. By plotting excavation depth against Mg/Si, we can determine if the signature is unique to the region.

2.5 Impact Depth of Excavation and Depth of Melting

Much work has been done on the depth of excavation and stratigraphic uplift caused by crater/basin formation on the Moon and Earth (Cintala & Grieve, 1998; Croft, 1985; Melosh, 1989; Potter et al., 2013). Croft (1985) explains that crater feature sizes can largely be scaled based on the simple-to-complex transition diameter, D_{sc}. Croft reasons that D_{sc} accounts for the differences in gravity and target composition and other structures rely largely on the transient crater diameter, D_t. Croft (1985) provides an equation for calculating D_t,

$$D_t = D_{sc}^{0.15\pm0.04} D_f^{0.85\pm0.04}, \qquad (8)$$

where $D_{sc} = 11.7$ km ± 1.2 km (Susorney et al., 2016) and D_f is the final crater diameter, taken from the Baker and Head catalogue. This equation was calculated from 4 independent data sets from the Moon and Earth, with $D_f \leq 1500$ km, and Croft (1985) states that the equation is a good first-order approximation for other Solar System bodies. Croft (1985) also noted that the errors in the exponents are probably much smaller but have been chosen to keep the exponent of D_f between 0.8 and 0.9 and to reflect the uncertainty in individual data points. Potter et al. (2013) give the maximum structural uplift as,

$$U_{MAX} = 0.075 D_t^{1.27}, \qquad (9)$$

derived from numerical simulations of basin-sized ($D_f = 200$ to ~1000 km) lunar analogue impacts, for three different thermal profiles, and the lunar and terrestrial data from Cintala and Grieve (1998), which covered 12 lunar ($D_f = 17.0$ to 51.5 km, and 136 km) and 24 terrestrial ($D_f = 4$ to 54 km, and 300 km) craters. Potter and Head (2016) use numerical simulations to model excavation depths for different size impactors (50 to 250 km) and velocities (15 to 50 km/s) appropriate for Mercury. Potter and Head (2016) assumed crust, mantle, and core compositions of basalt, dunite and iron, respectively. Also assuming a dunite impactor, Potter and Head (2016) give the mercurian excavation depth as,

$$Z_{ex} = 0.141 D_t. \qquad (10)$$

Cintala and Grieve (1998) give the depth of melting as,

$$Z_m = U_{MAX} + d_p, \tag{11}$$

where d_p is the distance from the pre-impact surface to the top of the central peak. Susorney et al. (2016) provide data on rim height (above pre-impact surface), crater depth (from rim height), and peak height (from crater floor), which is used to calculate d_p. Eq. 11 assumes that the maximum uplift occurs in the central peak, which originates below the depth of melting, however, this does not hold true for peak-ring basins. The displaced structural uplift (DSU) model of Kring et al. (2016), along with simulations by Potter et al. (2013), suggest that peak-ring material originates from depths much shallower than the transient crater depth, $d_t = D_t/3$ (Melosh, 1989).

To determine Z_m for Mercury (Eq. 11), we used data from Susorney et al. (2016). The crater depth and central uplift height were used to calculate d_p. Final diameter, D_f, and simple-to-complex transition diameter, D_{sc}, were used to determine D_t (Eq. 8) and subsequently U_{MAX} (Eq. 9) for all central-peak craters with the data to calculate d_p. We used D_f from Susorney et al. (2016), which differs slightly from Baker and Head (2013) due to differing techniques. We then found the best-fit power law, as per the analysis of Cintala and Grieve (1998), which we extrapolated to basin sized impacts (Figure 2). The power law determined is,

$$Z_m = 0.1471 D_t^{1.1127}. \tag{12}$$

3 Results

3.1 Distribution of Basins on Mercury

Figure 3 shows the distribution of PRBs from the Baker and Head catalogue, including the extent of ejecta deposits, coloured to indicate the degradation class. The 1σ-HMST and 2σ-HMST are also shown for reference. Figure 4 shows the count statistics of total impact structures that intersect the 2σ-HMST, the statistics for PRBs without ejecta blankets are given in Figure S9. Full statistics are given in Table S3. Figure 4 shows the statistics for total impact structures (TIS) that intersect the 2σ-HMST. TIS are divided into degradation class and also grouped from all to freshest, to investigate how increasing freshness effects the statistics. The planetary mean and standard deviation (SD), derived from the random point statistics, are shown for comparison, and the confidence in the TIS count being greater-than-mean is also shown. It can be seen from Figure 4 that there is an over-density (15 out of 110) of TIS that intersect the 2σ-HMST, which is dominated by C2 and C3 PRBs. Although there are zero C1 basins intersecting the 2σ-HMST, this count is within 1 SD of the planetary mean, therefore unremarkable. The fifteen basins named in Figure 6 will be referred to as "The 15 Basins", to simplify discussion. It should be noted that Jobim is included as it meets the requirements but the basin largely exists outside of the 1σ-HMST.

Figure 5 shows the confidence level for each random sample point having greater-than-mean counts for C1 and C2 TIS that intersect a 926 km radius buffer, centred on the sample point. There are three obvious regions with high-confidence. First, the region in the vicinity of the HMST has confidences >99.87 % (3σ-5σ confidence), whilst the region centred on ~45°E, 5°N (Nabokov cluster), coincident with the southern part of the Nabokov region, has confidence from 84.1 % to 99.87 % (1σ-3σ confidence). The region centred on ~40°E, 50°N (Borealis

Planitia cluster) lies within Borealis Planitia and also has confidence from 84.1 % to 99.87 %. The Nabokov cluster has mean Mg/Si = 0.472 ± 0.022 and the Borealis Planitia cluster has mean Mg/Si = 0.372 ± 0.071. Confidence maps were also produced for different scenarios and it was found that the 3σ-5σ confidence in an over-density of craters coinciding with the HMT is unique to PRBs. This is asserted through comparison with N(20), N(50), and N(84 to 320) distributions in the Fassett data set, and with central-peak craters (CPCs) and protobasins from the Baker and Head data (Figures S10 and S11).

We therefore conclude that there is an over-density of PRBs in the vicinity of the HMT and this distribution does not coincide with the general N(20) crater population, craters of a similar size, or craters with a different morphology. Thus, the correlation is unique to PRBs and the HMT.

3.2 Uniqueness of Correlation

The probability of random alignment was calculated for 4 scenarios, shown in Table 3. PRBs and TISs were investigated for all degradation classes and C1/C2 classes. The region under analysis was determined as the region with ≥ 2σ confidence of a greater-than-mean basin count. The 2σ-HMST was used for all analyses. Table 3 clearly shows that the region with an over-density of C1 and C2 basins has a better alignment with the 2σ-HMST than when considering all basins. There is also a slight improvement when considering TIS rather than basin interiors only. Therefore, we can assert that a region with an over-density of fresh (C1 and C2) basins has a ≤ 0.51 % probability of randomly coinciding with the 2σ-HMST, assuming an omnidirectional impactor flux.

Figure 6 shows the basin interior Mg/Si values for The 15 Basins and all similar basins (Section 2.5). Table S4 shows the basins plotted and their Mg/Si values. The mean value for The 15 Basins is 0.649, whilst the mean for the similar population is 0.432. The planetary mean is 0.436 (Nittler et al., 2018) and the mean for the 2σ-HMST, calculated in a Mollweide projection, is 0.676. It can therefore be stated that similar PRBs across Mercury have a Mg/Si similar to the planetary mean, whilst The 15 Basins have elevated Mg/Si, with a mean value lower than the regional mean. Thus, we conclude that the high-Mg/Si material is unique to the region, and hence is laterally inhomogeneous throughout the crust.

3.3 Basin Excavation and Uplift Depths

Figure 7 shows the calculated depths of excavation, melting, and the transient crater. None of The 15 Basins have excavated mantle material and only five (Al-Hamadhani, Larrocha, Sholem Aleichem, Vivaldi, Vyasa) potentially melted mantle material during impact. Vyasa is the only basin that might have a large fraction of mantle in the melted material.

Separate analysis of the Mg/Si for basin floors and ejecta blankets (Table 2) did not indicate any strong variability, except for Vyasa, Jobim, and Sholem Aleichem, which exhibit differences of >0.05 Mg/Si. Vyasa and Sholem Aleichem both exhibit higher Mg/Si within the basin rim and Jobim shows greater Mg/Si in the ejecta blanket. When examining the TIS, there is a general reduction in Mg/Si as we move from C2 to C4 PRBs. This reduction is also observed when analyzing the ejecta blankets, although the use of a circle to define the ejecta blanket inevitably includes material that is not actually ejecta, which may be responsible for the apparent reduction. When solely examining basins, the only PRB to not exhibit this trend is Vyasa. Generally, with the exception of Vyasa, this trend could be taken as evidence that subsequent

impacts have diluted the Mg/Si signature, which is caused by the PRBs, through local gardening of ejecta overlaid on material with a different composition. In this scenario, gardening would not affect the composition within the basin walls. However, poor R^2 values are associated with linear, power-law, or polynomial fits when plotting Mg/Si values against basin features, degradation class, or initial crustal thickness. This precludes a firm conclusion based on available observational evidence. However, we can conclude that the Mg/Si signature is unlikely to be solely due to the excavation and exposure of mantle material. No variability with predicted depth is currently detectable. However, this does not preclude high-Mg/Si material being excavated and overlaid on an initial surface. In this scenario, PRBs have excavated and distributed high-Mg/Si crustal material across the HMT region.

4 Discussion

4.1 Distribution of Basins on Mercury

From the results in Section 3 it can be seen that there is an over-density of PRBs in the vicinity of the HMT. Although the count of basins intersecting the HMT is relatively low, the global statistics were collected from 10,000 random samples and therefore the HMT statistics are considered robust. The over-density is shown to be unique to PRBs and does not follow N(20) or N(50) crater population densities (Fassett catalogue), or population densities for all craters ≥ 50km diameter with a central peak or peak-ring structure (Baker and Head catalogue). Analysis was focused on PRBs that have an ejecta blanket that intersects the 2σ-HMST, which includes PRBs that heavily contribute to the 1σ-HMST signature, whilst disregarding PRBs on the periphery of the 1σ-HMST. Jobim is included as it meets the criteria, although the basin is largely outside the 1σ-HMST. This makes it an interesting candidate for further observations. This over-density is found to coincide with the 2σ-HMST with a probability of being random of just 1.98% for all TIS and 0.51 % for C1 and C2 TIS. So there is strong evidence of a correlation between the HMT and an over-density of PRBs, which seems to be dominated by C2 and C3 PRBs. Although there are no C1 PRBs intersecting the 2σ-HMST, this is within 1 SD of the planetary mean and therefore not considered significant. When excluding the ejecta blankets, the only marked difference is a lower confidence (~62 %) in an over-density of C3 basins. The higher confidences, when including ejecta blankets, implies that they are important to the correlation.

By definition, C2 PRBs will have undergone less local gardening and proximal degradation than C3 basins, so the signature will have been diluted less than in other regions. This leads to a simple conclusion that an over-abundance of fresher material is responsible for the high-Mg/Si signature, caused by the large number of PRBs in the region. However, this assumes that the high-Mg/Si material is ubiquitous across the surface of Mercury. Investigation of similar impacts across Mercury indicates that the mean Mg/Si for similar PRBs is close to the planetary mean. Even with a lower density of PRBs, an elevated Mg/Si signature should be detectable at PRB scales, if it is present, suggesting that the high-Mg/Si material is likely inhomogeneous at depth, as well as on the surface. Weider et al. (2015) suggest that a laterally and vertically heterogeneous mantle could explain the surface inhomogeneity. However, a poorly mixed mantle (Frank et al., 2017) or stratified magma ocean (McCoy et al., 2018) could both explain the surface inhomogeneity. There are two other regions with a high-density of PRBs,

Nabokov (centred on ~45°E, 5°N; Figure 5) and Borealis Planitia (centred on ~40°E, 50°N; Figure 5), but no correlation was found on scales of the 2σ-HMST. There is a region of high-Fe/Si in the vicinity of Nabokov (Nittler et al., 2018) but, due to a large instrument footprint and low abundances of Fe, the high-Fe/Si region is poorly defined. Thus, no sensible numerical analysis can be performed without further investigation when MIXS returns higher-resolution and/or higher sensitivity data. It is worth noting that elevated Fe/Si has also been detected in the HMT, making this another high priority for follow on measurements with MIXS.

The International Ocean Discovery Program, expedition 364, confirmed the DSU model (Morgan et al., 2016), which indicates that the peak-ring material does not originate from below the melt cavity. However, we can assume that excavated material is located in the ejecta blanket and the remaining melted material is still within the basin rim. Investigation of the difference in Mg/Si values between basins and ejecta blankets showed little variability, except for Vyasa, Sholem Aleichem, and Jobim. It should be noted that Vyasa is a C4 PRB and its ejecta blanket is overlain by other impacts (Figure 3). The basin of Sholem Aleichem intersects the basin of Vyasa, with the ejecta of Sholem Aleichem extending across the basin of Vyasa. As Sholem Aleichem is fresher (C3) than Vyasa (C4), Vyasa has likely been largely overlaid by Sholem Aleichem's ejecta and then subsequently gardened. Therefore the variability seen within Vyasa needs to be treated with caution and should be subject to further investigation with MIXS. The variability seen in Jobim may be due to different material being present and it is worth noting that the impact is into a region of greater elevation and crustal thickness than the other 14 basins, with the exceptions of Praxiteles and Baker 91. Praxiteles has similar Mg/Si values within the basin and ejecta blanket, whilst Baker 91 has an ejecta Mg/Si value slightly greater (~0.02) than the basin value (Table 2). Croft (1985) was used to calculate the transient crater diameter, as this was consistent with the work of Potter et al. (2013). Holsapple (1993) present a different scaling relationship, derived from measurements rather than an assumed hemispherical shape (Croft, 1985):

$$D_t = 0.758 D_{sc}^{0.079} D_f^{0.921}. \qquad (13)$$

Holsapple consistently predicts a lower transient crater diameter (~9 km across the final diameter range of 84 to 320 km), so the values given in Figure 6 might be expected to be lower. This essentially rules out an excavated mantle origin for the Mg/Si material, which available evidence suggests is likely present at all crustal depths within the HMT.

Wieczorek et al. (2012) hypothesize that Mercury has not always been in a 3:2 resonant orbit but was initially in a synchronous orbit, with a large impact subsequently shifting it to the current orbit. They predict that this would lead to a region of low-frequency impacts for basins with diameters ≥100 km, during the synchronous period. They present evidence that a region with a low density of basins with diameters ≥400 km supports their hypothesis. Using the centres of 3 large basins (Sobkou, 33.4N -133.5E; Matisse-Repin, -23.4N -75.2E; Derzhavin-Sor Juan, 50.8N -26.9E) to define a circle, this region is centred on 24.3N -79.2E with a diameter of 4075 km. The probability of this region coinciding with the 2σ-HMST and the over-density of fresh (C1 and C2) TISs is calculated to be 0.51 %. To calculate this value, the centre-point for each ROI was determined along with the mean centre-point for all three ROIs. The greatest probability of any ROI centre-point being collocated with the mean centre-point was then determined (Section 2.4). The high-density of PRBs in the region is compatible with Wieczorek et al. (2012), as the general freshness (C2 and C3) of the PRBs would indicate their formation after the larger C5 basins, identified in Wieczorek et al. (2012), formed. This would place their

formation in the 3:2 orbital period, which occurred after the synchronous period. Wieczorek et al. (2012) state that the last impact capable of directly moving the orbit from synchronous to 3:2 resonance is Caloris, which occurred 3.73 Gyr ago (Fassett et al., 2009).

It is still unclear why there is an over-density of fresh PRBs in this region but whatever the reason, it seems likely that the basins have excavated high-Mg/Si material from all depths of the crust. This material may have been overlaid on an initial surface with a different composition and subsequently been impact gardened. Thus, an over-abundance of fresh PRBs have revealed high-Mg/Si material in sufficient quantity to be detectable at large scales. The material has not been detected elsewhere, with the notable exception of Rachmaninoff, which implies it is laterally inhomogeneous. This observation is limited by the coarse resolution of the MESSENGER XRS and Gamma-ray and Neutron Spectrometer instruments, therefore small regions with elevated Mg/Si may exist. The HMT is believed to be an old terrane, forming part of the Vivaldi region (Denevi et al., 2018), but if Wieczorek et al. (2012) are correct, then the region did not undergo major resurfacing due to large ($\geq$400 km diameter) basin impacts. The formation of the Borealis Planitia resurfaced a large region of Mercury, along with the Caloris impact (Denevi et al., 2013), but neither of these events resurfaced the HMT. It is plausible that the only major resurfacing events in this region have been the formation of The 15 Basins. There are other regions that have undergone little major resurfacing, such as the Nabokov region (Denevi et al., 2018), which apparently has greater-than-mean Mg/Si but with a low (~50 %) statistical confidence. An over-density of PRBs has been identified in the south of this region but with a lower statistical significance. It is unclear if the lack of PRBs is responsible for the close-to-mean Mg/Si values. XRS can only detect elements in the upper ~100 μm of the surface, so the signature could easily be masked by impact gardening and the lack of PRBs may mean that not enough material has been excavated to cause an elevated Mg/Si signature in the manner seen in the HMST. Alternatively, the lack of high Mg/Si in the Nabokov region may offer evidence that the early crust was indeed inhomogeneous, though the remarkably low probability of chance coalignments of the geochemical contours and the over-density of PRBs seem to imply some kind of causal link.

4.2 Rachmaninoff Basin

Some evidence for this basin having a high-Mg/Si composition comes from a small 1.5σ-Mg/Si contour that exists within the rim of Rachmaninoff Basin (Figure 8). However, due to the low resolution of the XRS instrument, the relative error in the contour is large compared to the size of the region enclosed by the contour. Using the methods from Section 2.4, we calculate that the probability of the 1.5σ-contour randomly coinciding with Rachmaninoff is $\lesssim 3\times10^{-3}$ %. The 1σ-Mg/Si contour extends to the ejecta blanket with a lobe to the south-west, where it partially coincides with a topographic low and smooth plains units, identified by Denevi et al. (2013) and Kinczyk et al. (2018). Whitten and Head (2015) identified smooth plains overlaying the ejecta blanket to the south-west of the basin, indicating the projectile probably came from the north-east (Chapman et al., 2018). There is a slight reddening of the material within the topographic low to the south-west, but generally it is the same colour as the surrounding terrain, indicating that the exterior plains are most likely the product of impact melt, rather than volcanic extrusion (Denevi et al., 2018). All of this data support a hypothesis that the one-sigma contour is caused by ejecta from the formation of Rachmaninoff, with pooled impact melt gathering in the topographic low and causing the smooth plain units coincident with the contour lobe.

As one of the largest basins to retain its peak-ring and being C1 fresh, Rachmaninoff may offer some insight into the observed correlation of PRBs with the HMT. The initial crustal thickness for the Rachmaninoff impact is estimated to be ~35 km (see Figure 7). No mantle material appears to have been excavated, however, the depth of melting reaches a maximum of ~48 km, which is comparable to Vyasa. Cintala and Grieve (1998) give the melt volume as

$$V_m = cD_t^{3.85}, \qquad (14)$$

where $c = 1.67 \times 10^{-4}$ is a unit-less constant indicating a chondritic impactor travelling at a speed of 40 km s^{-1}, and the mean impact velocity for Mercury is 42.5 km s^{-1} (Le Feuvre & Wieczorek, 2008). From Cintala and Grieve (1998) we estimate ~42% of the melt volume is ejected, then using Croft (1985) to calculate D_t (Eq. 8) gives

$$V_e = 0.42V_m = 33,933^{+93,679}_{-24,674} km^3. \qquad (15)$$

For comparison, if we use Holsapple (1993) to calculate D_t (Eq. 15), we get the ejected volume as $V_e = 28,173 \ km^3$.

So, within the error bounds given by Croft (1985) and assuming that the equations can be applied to Mercury, between ~9000 km^3 and ~127,000 km^3 of material was ejected from Rachmaninoff during formation, although a figure of ~30,000 km^3 is more likely. Some of this material may have pooled in a topographic low to the south-west of the basin. Rachmaninoff suggests that the crustal material has elevated Mg/Si whilst the greater Mg/Si within the basin suggests that the Mg/Si signature is more prevalent at greater depths, possibly with a large contribution from the mantle (Figure 7). This is supported by Vyasa but heavy degradation means the signature needs further investigation in that region. We suggest further observations, by MIXS, are also required for Rachmaninoff and the surrounding regions.

4.3 Future Work: MIXS Targeting

The MIXS instrument, onboard BepiColombo, is well placed to build on MESSENGER results using its two channels, MIXS-C and MIXS-T. MIXS-C is a collimated instrument with a 10.4° FOV giving a footprint of ~70 km at periherm and ~270 km at apoherm. MIXS-T is an imaging telescope with a 1.1° FOV, providing an angular resolution < 9 arcmin. During elevated solar-flare states, MIXS-T could provide resolutions of the order 1–4 km (Fraser et al., 2010). MIXS-T will have the capability to image crater features and other geological features during periods of intense solar activity, however, the regions covered will be serendipitous. Thus, to ensure the most valuable data are secured, targets need to be prioritised.

The MIXS crater catalogue has been completed and is presented in supplementary material, but this is only the first step in prioritising targets for MIXS. Large craters can be more easily imaged and fresh craters are more likely to reveal the stratigraphy of the crater as degradation has not yet masked geochemical signatures. A new system for X-ray analysis is also being developed which will allow the detectability of elements (by photon count) to be examined. Latitude affects the intensity of the surface solar flux, so this effect also needs to be factored into target prioritisation. Instrument dwell time and solar state will strongly impact the number of photons collected in any given region. Orbital analysis needs to be carried out, to determine which regions offer the most favourable conditions, during intense solar flare events, to reveal low element abundances and the highest sensitivity measurements of major-element ratios. These measurements need to be collected from spatial scales relevant to individual impact

features right through to regional features like the HMST. This work will be included in a prioritised list of targets for MIXS. However, given current knowledge from MESSENGER, it is apparent that the basins in the HMT and superficially similar basins (Table S4) within other Mercury terranes need to be investigated further. Thus it is proposed that the basins Boethius, Polygnotus, Baker 18, Scarlatti, Baker 27, Jobim, Wang Meng, Al-Hamadhani, Aksakov, Praxiteles, Larrocha, Sholem Aleichem, Vivaldi, Baker 91, Vyasa, and Rachmaninoff are prioritized for MIXS observation.

The other regions with a moderate-confidence identified for an over-density of PRBs (Figure 5) do not appear to coincide definitively with other known features. The Nabokov cluster loosely coincides with a region of relatively high-Fe/Si but due to low absolute abundances and incomplete data for Fe/Si, robust statistical analysis is not possible based on the MESSENGER data set. This region varies more across the different selection criteria and it is noted that the crust is thicker in this region than in the HMT. Further observations are required to ascertain a correspondence between basin densities and Fe/Si in this region. Intriguingly, the 2σ-HMST and Nabokov cluster both appear to loosely coincide with regions of high fast neutron counts, identified by Lawrence et al. (2017). Further observations by BepiColombo will allow detailed investigation of this correlation. No corresponding features were identified in the vicinity of the Borealis Planitia cluster.

The Rachmaninoff case-study (Section 4.2) is informative but further work also needs to be done to properly understand the crater forming process on Mercury, rather than relying on lunar and terrestrial analogies. Although the equations used are broadly applicable, more definitive equations for Mercury would allow more accurate investigations of the depth of origin of crater material. As one of the largest basins to retain its peak-ring and being C1 fresh, Rachmaninoff may offer some insight into the observed correlation of PRBs with the HMT, therefore it is proposed that Rachmaninoff is also prioritized for MIXS observation.

To complete the analysis reported here, additional data needs to be acquired to ascertain whether the statistical correlations really can be used to inform the origin of the HMT. The key data set to enable this work will come from MIXS once BepiColombo enters its science phase (Bunce et al., 2020). MIXS-C will give more sensitive abundances at resolutions comparable to the best achieved by MESSENGER during its main science mission, MIXS-T will provide imaging resolutions which will enable analysis of large crater features in regions illuminated by bright solar flares. Resolutions of ~10 km per pixel should allow the imaging of structural features within PRBs, enabling more comprehensive case studies of basins, like Rachmaninoff, than has been possible here. In turn, the data will offer insight into the depths of origin of the different materials. Better high/low statistical contours can also be derived from higher resolution data, which will assist investigations into the real significance of the basin over-density.

5 Conclusions

A catalogue of all craters that retain a central peak or peak-ring structure ('MIXS crater catalogue') was created to aid in target prioritisation for BepiColombo's Mercury Imaging X-ray Spectrometer (MIXS). The catalogue was created by visually inspecting images from the MESSENGER mission. A correlation was noted between basins that retain their peak-ring structure and a region of Mercury that has high-Mg/Si values, the High Magnesium-Silicon Terrane (HMST). This correlation has been investigated, with reference to two other crater

catalogues: A catalogue of peak-ring, proto-, and ring-cluster basins by Baker and Head (2013), produced using morphometric methods; and a catalogue of craters with diameter ≥20 km by Fassett et al. (2012).

Robust statistical analysis was carried out by defining the HMST as a confidence contour using the mean and standard error values for Mg/Si, taken from Nittler et al. (2018) (Figure 1 and Table 1), and calculating mean and standard deviation crater counts from 10,000 randomly placed buffers, with areas equal to that enclosed by each of the confidence contours (Table 1). Analysis across all data sets revealed a strong correlation, ≥ 97.68 % confidence level, between basins that appeared in the Baker and Head catalogue, and the Mg/Si mean+2σ confidence region (2σ-HMST; see Figure 5). The high-confidence of the correlation existed with all selection criteria (Table 3), but not with the Fassett catalogue (Figure S11). The highest probability of random alignment, assuming an omnidirectional flux of impactors, is just 2.39 %. The absence of the correlation in the Fassett catalogue indicates that the correlation is due to basins only and not craters of a similar size. This is reinforced by the confidence level being lower if protobasins and ring-cluster basins are included. Hence, it is concluded that peak-ring basins heavily contribute to the HMST signature.

An investigation of material excavation and uplift revealed that 15 Basins within the 2σ-HMST (Boethius, Polygnotus, Baker 18, Scarlatti, Baker 27, Jobim, Wang Meng, Al-Hamadhani, Aksakov, Praxiteles, Larrocha, Sholem Aleichem, Vivaldi, Baker 91, and Vyasa) all excavated material from depths of >10 km. Only 5 of these basins (Al-Hamadhani, Larrocha, Sholem Aleichem, Vivaldi, and Vyasa) melted mantle material during formation, with only Vyasa potentially including a large proportion of mantle material in the impact melt. This essentially rules out a solely mantle origin for the Mg/Si material, which available evidence suggests is likely present at all sub-surface crustal depths within the HMST. The absence of high-Mg/Si material elsewhere on the surface suggests that the material is inhomogenous in the lower crust. Separate analysis of the Mg/Si for basin floors and ejecta blankets (Table 2) did not indicate any strong variability, except for Vyasa, Jobim, and Sholem Aleichem, which exhibit differences of >0.05 Mg/Si. Vyasa and Sholem Aleichem both exhibit higher Mg/Si within the basin rim and Jobim shows greater Mg/Si in the ejecta blanket. Rachmaninoff basin is particularly large (~300 km diameter) and fresh (C1 degradation class) and inconclusive evidence suggests that the Mg/Si signature increases with depth and is potentially present in mantle material. Further investigation is required to assess this conclusion more carefully.

Although the statistical correlation has a high confidence level, further work is required to determine the exact nature of the causal relationship between peak-ring basins and the HMST. To this end, it is proposed that the basins Boethius, Polygnotus, Baker 18, Scarlatti, Baker 27, Jobim, Wang Meng, Al-Hamadhani, Aksakov, Praxiteles, Larrocha, Sholem Aleichem, Vivaldi, Baker 91, Vyasa, and Rachmaninoff are all prioritized for MIXS observation when the science mission begins.

named reviewers, David Baker, Tim McCoy, and Hannah Susorney, for detailed and constructive comments that have substantially improved the paper.

The MIXS crater catalogue created as part of this work is archived in Hall et al. (2020)

Crater catalogues used for this research are included in these papers (and their supplementary information files): Baker and Head (2013), Fassett et al. (2012), and Susorney et al. (2016).

Mercurian surface composition data (Messenger XRS) can be found in Nittler (2016).

References

Baker, D. M. H., & Head, J. W. (2013). New morphometric measurements of craters and basins on Mercury and the Moon from MESSENGER and LRO altimetry and image data: An observational framework for evaluating models of peak-ring basin formation. *Planetary and Space Science, 86*, 91-116. doi: https://doi.org/10.1016/j.pss.2013.07.003

Baker, D. M. H., & Head, J. W. (2015). Constraints on the depths of origin of peak rings on the Moon from Moon Mineralogy Mapper data. *Icarus, 258*, 164-180. doi: https://doi.org/10.1016/j.icarus.2015.06.013

Baker, D. M. H., Head, J. W., Schon, S. C., Ernst, C. M., Prockter, L. M., Murchie, S. L., et al. (2011). The transition from complex crater to peak-ring basin on Mercury: New observations from MESSENGER flyby data and constraints on basin formation models. *Planetary and Space Science, 59*(15), 1932-1948. doi: https://doi.org/10.1016/j.pss.2011.05.010

Becker, K. J., Robinson, M. S., Becker, T. L., Weller, L. A., Edmundson, K. L., Neumann, G. A., et al. (2016). *First Global Digital Elevation Model of Mercury*. Paper presented at the 47th Lunar and Planetary Science Conference.

Benkhoff, J., van Casteren, J., Hayakawa, H., Fujimoto, M., Laakso, H., Novara, M., et al. (2010). BepiColombo—Comprehensive exploration of Mercury: Mission overview and science goals. *Planetary and Space Science, 58*(1), 2-20. doi: https://doi.org/10.1016/j.pss.2009.09.020

Bunce, E. J., Martindale, A., Lindsay, S., Muinonen, K., Rothery, D. A., Pearson, J., et al. (2020). The BepiColombo Mercury Imaging X-Ray Spectrometer: Science Goals, Instrument Performance and Operations. *Space Science Reviews, 216*(8), 126. doi: 10.1007/s11214-020-00750-2

Chapman, C. R., Baker, D. M. H., Barnouin, O. S., Fassett Caleb, I., Marchi, S., Merline, W. J., et al. (2018). Impact Cratering of Mercury. In B. J. Anderson, L. R. Nittler, & S. C. Solomon (Eds.), *Mercury: The View after MESSENGER* (pp. 217-248). Cambridge: Cambridge University Press.

Cintala, M. J., & Grieve, R. A. F. (1998). Scaling impact melting and crater dimensions: Implications for the lunar cratering record. *Meteoritics & Planetary Science, 33*(4), 889-912. doi: 10.1111/j.1945-5100.1998.tb01695.x

Croft, S. K. (1985). The scaling of complex craters. *Journal of Geophysical Research: Solid Earth, 90*(S02), C828-C842. doi: 10.1029/JB090iS02p0C828

Denevi, B. W., Chabot, N. L., Murchie, S. L., Becker, K. J., Blewett, D. T., Domingue, D. L., et al. (2017). Calibration, Projection, and Final Image Products of MESSENGER's Mercury Dual Imaging System. *Space Science Reviews, 214*(1), 2. doi: 10.1007/s11214-017-0440-y

Denevi, B. W., Ernst, C. M., Meyer, H. M., Robinson, M. S., Murchie, S. L., Whitten, J. L., et al. (2013). The distribution and origin of smooth plains on Mercury. *Journal of Geophysical Research: Planets, 118*(5), 891-907. doi: 10.1002/jgre.20075

Denevi, B. W., Ernst, C. M., Prockter, L. M., & Robinson, M. S. (2018). The Geologic History of Mercury. In B. J. Anderson, L. R. Nittler, & S. C. Solomon (Eds.), *Mercury: The View after MESSENGER* (pp. 144-175). Cambridge: Cambridge University Press.

Fassett, C. I., Head, J. W., Baker, D. M. H., Zuber, M. T., Smith, D. E., Neumann, G. A., et al. (2012). Large impact basins on Mercury: Global distribution, characteristics, and modification history from MESSENGER orbital data. *Journal of Geophysical Research: Planets, 117*(E12). doi: 10.1029/2012JE004154

Fassett, C. I., Head, J. W., Blewett, D. T., Chapman, C. R., Dickson, J. L., Murchie, S. L., et al. (2009). Caloris impact basin: Exterior geomorphology, stratigraphy, morphometry, radial sculpture, and smooth plains deposits. *Earth and Planetary Science Letters, 285*(3), 297-308. doi: https://doi.org/10.1016/j.epsl.2009.05.022

Fassett, C. I., Kadish, S. J., Head, J. W., Solomon, S. C., & Strom, R. G. (2011). The global population of large craters on Mercury and comparison with the Moon. *Geophysical Research Letters, 38*(10). doi: 10.1029/2011GL047294

Frank, E. A., Potter, R. W. K., Abramov, O., James, P. B., Klima, R. L., Mojzsis, S. J., & Nittler, L. R. (2017). Evaluating an impact origin for Mercury's high- magnesium region. *Journal of Geophysical Research: Planets, 122*(3), 614-632. doi: 10.1002/2016JE005244

Fraser, G. W., Carpenter, J. D., Rothery, D. A., Pearson, J. F., Martindale, A., Huovelin, J., et al. (2010). The mercury imaging X-ray spectrometer (MIXS) on bepicolombo. *Planetary and Space Science, 58*(1-2), 79-95. doi: 10.1016/j.pss.2009.05.004

Genova, A., Goossens, S., Mazarico, E., Lemoine, F. G., Neumann, G. A., Kuang, W., et al. (2019). Geodetic Evidence That Mercury Has A Solid Inner Core. *Geophysical Research Letters, 46*(7), 3625-3633. doi: 10.1029/2018GL081135

Goldsten, J. O., Rhodes, E. A., Boynton, W. V., Feldman, W. C., Lawrence, D. J., Trombka, J. I., et al. (2007). The MESSENGER Gamma-Ray and Neutron Spectrometer. *Space Science Reviews, 131*(1), 339-391. doi: 10.1007/s11214-007-9262-7

Grieve, R. A. F. (1987). Terrestrial Impact Structures. *Annual Review of Earth and Planetary Sciences, 15*(1), 245-270. doi: 10.1146/annurev.ea.15.050187.001333

Hall, G. P., Martindale, A., Bridges, J. C., Nittler, L. R., & Bunce, E. J. (2020). *MIXS Crater Catalogue [Data set]*. University of Leicester. https://doi.org/10.25392/LEICESTER.DATA.12045216.V1

Herrick, R. R., Bateman, E. M., Crumpacker, W. G., & Bates, D. (2018). Observations From a Global Database of Impact Craters on Mercury With Diameters Greater than 5 km. *Journal of Geophysical Research: Planets, 123*(8), 2089-2109. doi: 10.1029/2017JE005516

Holsapple, K. A. (1993). The Scaling of Impact Processes in Planetary Sciences. *Annual Review of Earth and Planetary Sciences, 21*(1), 333-373. doi: 10.1146/annurev.ea.21.050193.002001

Kinczyk, M. J., Prockter, L. M., Byrne, P. K., Denevi, B. W., Ostrach, L. R., & Skinner, J. A. (2018). *A Global Geological Map of Mercury*. Paper presented at the Mercury: Current and Future Science 2018.

Kinczyk, M. J., Prockter, L. M., Byrne, P. K., Susorney, H. C. M., & Chapman, C. R. (2020). A morphological evaluation of crater degradation on Mercury: Revisiting crater classification with MESSENGER data. *Icarus, 341*, 113637. doi: https://doi.org/10.1016/j.icarus.2020.113637

Klima, R. L., Denevi, B. W., Ernst, C. M., Murchie, S. L., & Peplowski, P. N. (2018). Global Distribution and Spectral Properties of Low-Reflectance Material on Mercury. *Geophysical Research Letters, 45*(7), 2945-2953. doi: 10.1002/2018GL077544

Kneissl, T., Michael, G. G., Platz, T., & Walter, S. H. G. (2015). Age determination of linear surface features using the Buffered Crater Counting approach – Case studies of the Sirenum and Fortuna Fossae graben systems on Mars. *Icarus, 250*, 384-394. doi: https://doi.org/10.1016/j.icarus.2014.12.008

Kring, D. A., Kramer, G. Y., Collins, G. S., Potter, R. W. K., & Chandnani, M. (2016). Peak-ring structure and kinematics from a multi-disciplinary study of the Schrödinger impact basin. *Nature Communications, 7*(1), 13161. doi: 10.1038/ncomms13161

Lawrence, D. J., Peplowski, P. N., Beck, A. W., Feldman, W. C., Frank, E. A., McCoy, T. J., et al. (2017). Compositional terranes on Mercury: Information from fast neutrons. *Icarus, 281*, 32-45. doi: https://doi.org/10.1016/j.icarus.2016.07.018

Le Feuvre, M., & Wieczorek, M. A. (2008). Nonuniform cratering of the terrestrial planets. *Icarus, 197*(1), 291-306. doi: https://doi.org/10.1016/j.icarus.2008.04.011

Marchi, S., Chapman, C. R., Fassett, C. I., Head, J. W., Bottke, W. F., & Strom, R. G. (2013). Global resurfacing of Mercury 4.0–4.1 billion years ago by heavy bombardment and volcanism. *Nature, 499*, 59. doi: 10.1038/nature12280
https://www.nature.com/articles/nature12280#supplementary-information

McCoy, T. J., Peplowski, P. N., McCubbin, F. M., & Weider, S. Z. (2018). The Geochemical and Mineralogical Diversity of Mercury. In B. J. Anderson, L. R. Nittler, & S. C. Solomon (Eds.), *Mercury: The View after MESSENGER* (pp. 176-190). Cambridge: Cambridge University Press.

Melosh, H. J. (1989). *Impact cratering : a geologic process*. New York : Oxford: Oxford University Press ; Clarendon Press.

Morgan, J. V., Gulick, S. P. S., Bralower, T., Chenot, E., Christeson, G., Claeys, P., et al. (2016). The formation of peak rings in large impact craters. *Science, 354*(6314), 878. doi: 10.1126/science.aah6561

Moriarty, D. P., Pieters, C. M., & Isaacson, P. J. (2013). Compositional heterogeneity of central peaks within the South Pole- Aitken Basin. *Journal of Geophysical Research: Planets, 118*(11), 2310-2322. doi: 10.1002/2013JE004376

Nittler, L. R. (2016). *MESSENGER XRS Derived (RDR) Data Bundle*. Geosciences Node. https://doi.org/10.17189/1518582

Nittler, L. R., Chabot, N. L., Grove, T. L., & Peplowski, P., N. (2018). The Chemical Composition of Mercury. In C. Solomon Sean, R. Nittler Larry, & B. J. Anderson (Eds.), *Mercury: The View After MESSENGER*. Cambridge, UK: Cambridge University Press.

Peplowski, P. N., Klima, R. L., Lawrence, D. J., Ernst, C. M., Denevi, B. W., Frank, E. A., et al. (2016). Remote sensing evidence for an ancient carbon-bearing crust on Mercury. *Nature Geoscience, 9*(4), 273-276. doi: 10.1038/ngeo2669

Peplowski, P. N., Lawrence, D. J., Rhodes, E. A., Sprague, A. L., McCoy, T. J., Denevi, B. W., et al. (2012). Variations in the abundances of potassium and thorium on the surface of Mercury: Results from the MESSENGER Gamma- Ray Spectrometer. *Journal of Geophysical Research: Planets, 117*(E12). doi: 10.1029/2012JE004141

Perry, M. E., Kahan, D. S., Barnouin, O. S., Ernst, C. M., Solomon, S. C., Zuber, M. T., et al. (2013). *Radio Frequency Occultations show that Mercury is Oblate*. Paper presented at the 44th Lunar and Planetary Science Conference, The Woodlands, Texas.

Phillips, R. J., Byrne, P. K., James, P. B., Mazarico, E., Neumann, G. A., & Perry, M. E. (2018). Mercury's Crust and Lithosphere: Structure and Mechanics. In B. J. Anderson, L. R. Nittler, & S. C. Solomon (Eds.), *Mercury: The View after MESSENGER* (pp. 52-84). Cambridge: Cambridge University Press.

Potter, R. W. K., & Head, J. W. (2016). *Lunar and Mercurian Imapact Basin Formation: Similar or Dissimilar? Insights from numerical modelling*. Paper presented at the 47th Lunar and Planetary Science Conference, The Woodlands, Texas.

Potter, R. W. K., Kring, D. A., & Collins, G. S. (2013). Quantifying the attenuation of structural uplift beneath large lunar craters. *Geophysical Research Letters, 40*(21), 5615-5620. doi: 10.1002/2013GL057829

Rivera-Valentin, E. G., & Barr, A. C. (2014). Impact-induced compositional variations on Mercury. *Earth and Planetary Science Letters, 391*, 234-242. doi: https://doi.org/10.1016/j.epsl.2014.02.003

Schlemm, C. E., Starr, R. D., Ho, G. C., Bechtold, K. E., Hamilton, S. A., Boldt, J. D., et al. (2007). The x-ray spectrometer on the MESSENGER spacecraft. *Space Science Reviews, 131*(1-4), 393-415. doi: 10.1007/s11214-007-9248-5

Solomon, S. C., & Anderson, B. J. (2018). The MESSENGER Mission: Science and Implementation Overview. In B. J. Anderson, L. R. Nittler, & S. C. Solomon (Eds.), *Mercury: The View after MESSENGER* (pp. 1-29). Cambridge: Cambridge University Press.

Song, E., Bandfield, J. L., Lucey, P. G., Greenhagen, B. T., & Paige, D. A. (2013). Bulk mineralogy of lunar crater central peaks via thermal infrared spectra from the Diviner Lunar Radiometer: A study of the Moon's crustal composition at depth. *Journal of Geophysical Research: Planets, 118*(4), 689-707. doi: 10.1002/jgre.20065

Spudis, P. D. (1993). *The Geology of Multi-Ring Impact Basins: The Moon and Other Planets*. Cambridge: Cambridge University Press.

Susorney, H. C. M., Barnouin, O. S., Ernst, C. M., & Johnson, C. L. (2016). Morphometry of impact craters on Mercury from MESSENGER altimetry and imaging. *Icarus, 271*, 180-193. doi: https://doi.org/10.1016/j.icarus.2016.01.022

Tompkins, S., & Pieters, C. M. (1999). Mineralogy of the lunar crust: Results from Clementine. *Meteoritics & Planetary Science, 34*(1), 25-41. doi: https://doi.org/10.1111/j.1945-5100.1999.tb01729.x

Vander Kaaden, K. E., & McCubbin, F. M. (2015). Exotic crust formation on Mercury: Consequences of a shallow, FeO-poor mantle. *Journal of Geophysical Research: Planets, 120*(2), 195-209. doi: 10.1002/2014JE004733

Weider, S. Z., Nittler, L. R., Starr, R. D., Crapster-Pregont, E. J., Peplowski, P. N., Denevi, B. W., et al. (2015). Evidence for geochemical terranes on Mercury: Global mapping of major elements with MESSENGER's X-Ray Spectrometer. *Earth and Planetary Science Letters, 416*(Supplement C), 109-120. doi: https://doi.org/10.1016/j.epsl.2015.01.023

Whitten, J. L., & Head, J. W. (2015). Rembrandt impact basin: Distinguishing between volcanic and impact-produced plains on Mercury. *Icarus, 258*, 350-365. doi: https://doi.org/10.1016/j.icarus.2015.06.022

Wieczorek, M. A., Correia, A. C. M., Le Feuvre, M., Laskar, J., & Rambaux, N. (2012). Mercury's spin–orbit resonance explained by initial retrograde and subsequent synchronous rotation. *Nature Geoscience, 5*(1), 18-21. doi: 10.1038/ngeo1350

Zuber, M. T., Smith, D. E., Phillips, R. J., Solomon, S. C., Neumann, G. A., Hauck, S. A., et al. (2012). Topography of the Northern Hemisphere of Mercury from MESSENGER Laser Altimetry. *Science, 336*(6078), 217. doi: 10.1126/science.1218805

Tables

Table 1 The confidence levels for rejecting H_0^C and the associated Mg/Si value. The regions for each Mg/Si value are shown in Figure 1.

Region	Area (km^2)	Value	Mg/Si value	Confidence level for rejecting H_0^C
1σ-HMST	8,204,131	$\mu^C + \sigma^C$	0.542	84.1 %
1.5σ-HMST	5,350,211	$\mu^C + 1.5\,\sigma^C$	0.595	93.3 %
2σ-HMST	2,693,840	$\mu^C + 2\,\sigma^C$	0.648	97.7 %

Table 2. Mean and standard deviation Mg/Si values for basin interior, ejecta blanket, and total impact structure. Baker ID, name, and centre coordinates are given to facilitate basin identification. MIXS crater catalogue ID is also given for cross-referencing purposes. (-) indicates that the basin does not appear in the MIXS crater catalogue.

Baker (MIXS) ID	Name	Long.	Lat.	Basin Mg/Si		Ejecta Mg/Si		TIS Mg/Si	
				Mean	SD	Mean	SD	Mean	SD
8 (1608)	Boethius	-73.51	-1.01	0.637	0.003	0.636	0.011	0.636	0.010
12 (1629)	Polygnotus	-69.21	-0.05	0.637	0.004	0.635	0.012	0.635	0.012
18 (-)	Baker 18	-108.52	18.41	0.614	0.010	0.617	0.025	0.617	0.024
24 (355)	Scarlatti	-101.37	40.58	0.635	0.022	0.629	0.030	0.630	0.029
27 (1730)	Baker 27	-53.25	18.70	0.629	0.005	0.625	0.013	0.625	0.013
31 (465)	Jobim	-66.69	32.65	0.531	0.019	0.587	0.037	0.580	0.039
37 (1428)	Wang Meng	-104.13	8.57	0.669	0.003	0.663	0.009	0.664	0.009
45 (388)	Al-Hamadhani	-91.94	38.93	0.640	0.026	0.659	0.042	0.656	0.041
54 (423)	Aksakov	-78.69	34.76	0.698	0.009	0.691	0.020	0.692	0.019
73 (487)	Praxiteles	-60.34	27.08	0.649	0.011	0.648	0.011	0.645	0.012
74 (452)	Larrocha	-69.81	43.39	0.675	0.015	0.661	0.042	0.663	0.040
78 (-)	Sholem Aleichem	-90.11	50.97	0.668	0.047	0.581	0.084	0.625	0.097
88 (1535)	Vivaldi	-85.81	13.60	0.679	0.003	0.675	0.006	0.675	0.006
91 (-)	Baker 91	-64.71	24.53	0.631	0.009	0.652	0.010	0.652	0.010
108 (-)	Vyasa	-84.79	49.87	0.742	0.020	0.582	0.149	0.582	0.149

Table 3. The probability of random alignment between regions with an over-density of PRBs and the 2σ-HMST. Four different definitions of basins are use, where the region used is defined as having > 2σ confidence that the basin count is greater-than-mean. Angular distance between

the centre-of-mass of the ROI and 2σ-HMST is given with the corresponding probability of random alignment.

Basin Definition	Basin Degradation Classes	Angular Distance Between Centre and 2σ-HMST Centre	Probability of Random Alignment with 2σ-HMST
Basin Interior	All	17.80°	2.39 %
Basin Interior	C1 and C2	6.52°	0.32 %
Total Impact Structure	All	16.20°	1.98 %
Total Impact Structure	C1 and C2	8.21°	0.51 %

Figures

Figure 1. The Mg/Si map for Mercury in Mollweide projection centred on 0° East, with longitudinal lines spaced at 30°. The contours for three different values of Mg/Si are shown. The confidence level for rejecting H_0^C within each contour is given in Table 1. MESSENGER XRS data from Nittler (2016).

Figure 2 - Depth of melting, Z_m, determined in this study from Susorney et al. (2016). The Lunar Z_m power law of Cintala and Grieve (1998) is also shown for comparison.

Figure 3 - Map of Baker and Head peak-ring basins, showing the basin (solid circle) and ejecta extent (open circle). PRB classifications are indicated by colour (see legend). The 1σ-HMST is delineated by a light-blue line and the 2σ-HMST is delineated by a black line. The map is shown in a Mollweide projection centred on 0°E.

Figure 4 - Bar chart showing the count statistics for total impact structures (TIS) that intersect the 2σ-HMST. TIS are divided into degradation class and also grouped from all to freshest. Counts are shown as blue bars, planetary means and SD are shown as black crosses and error bars, respectively. Both use the scale on the left-hand axis. The probability of the count being greater-than-mean is shown as red triangles, with the scale on the right-hand axis.

Figure 5. Confidence map for the data set Baker C1 and C2 TIS, with a 2σ-buffer size. The 10,000 random points indicate the centre of buffers, coloured to indicate the confidence level, ϵ, for rejecting H_0^B within each buffer. The map uses a Mollweide projection, centred on 0° East.
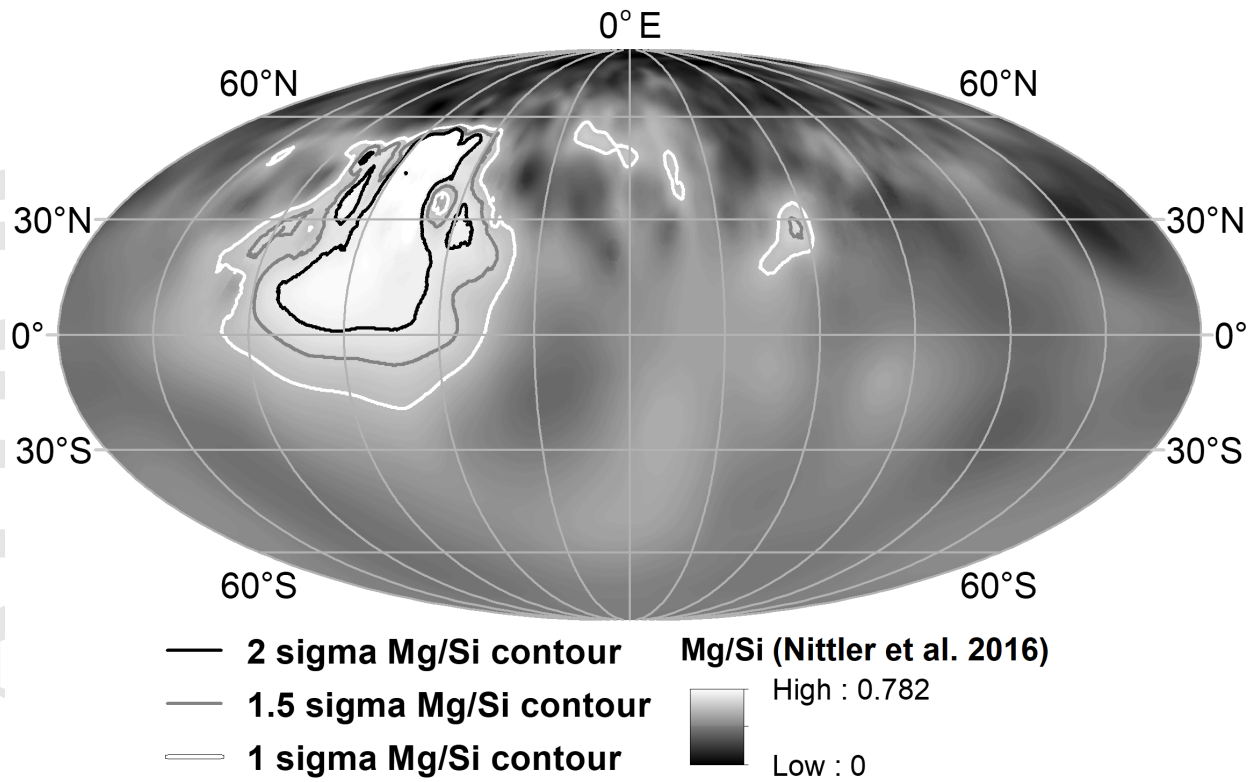
Figure 6. - Mg/Si values for the 15 basins intersecting the 2σ-HMST (red) and all similar basins (purple). Error bars are present for all points but are mostly too small to be observed. Depth of
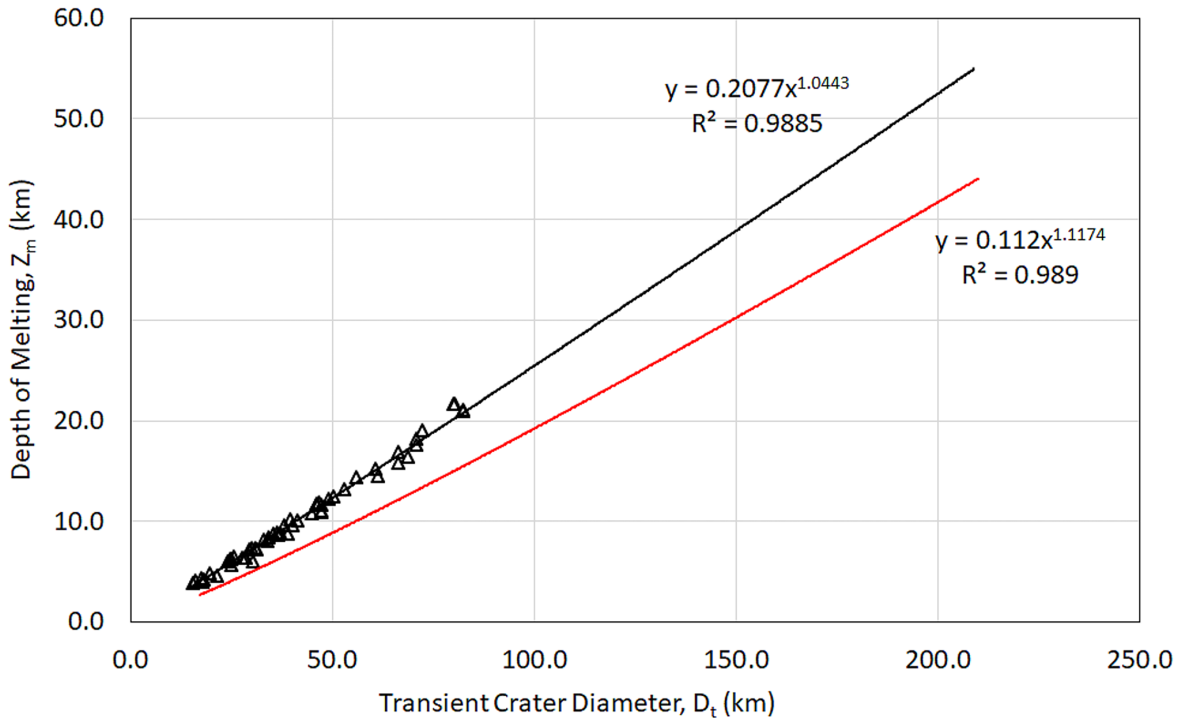
excavation is used as a proxy for basin size and allows the separation of data points, however its use is arbitrary. Population means are shown along with planetary mean and standard deviation.

Figure 7. Excavation depth, depth of melting, and transient crater depth plotted over crustal thickness for the 15 basins that intersect the 2σ-HMST. Rachmaninoff is included for discussion purposes.
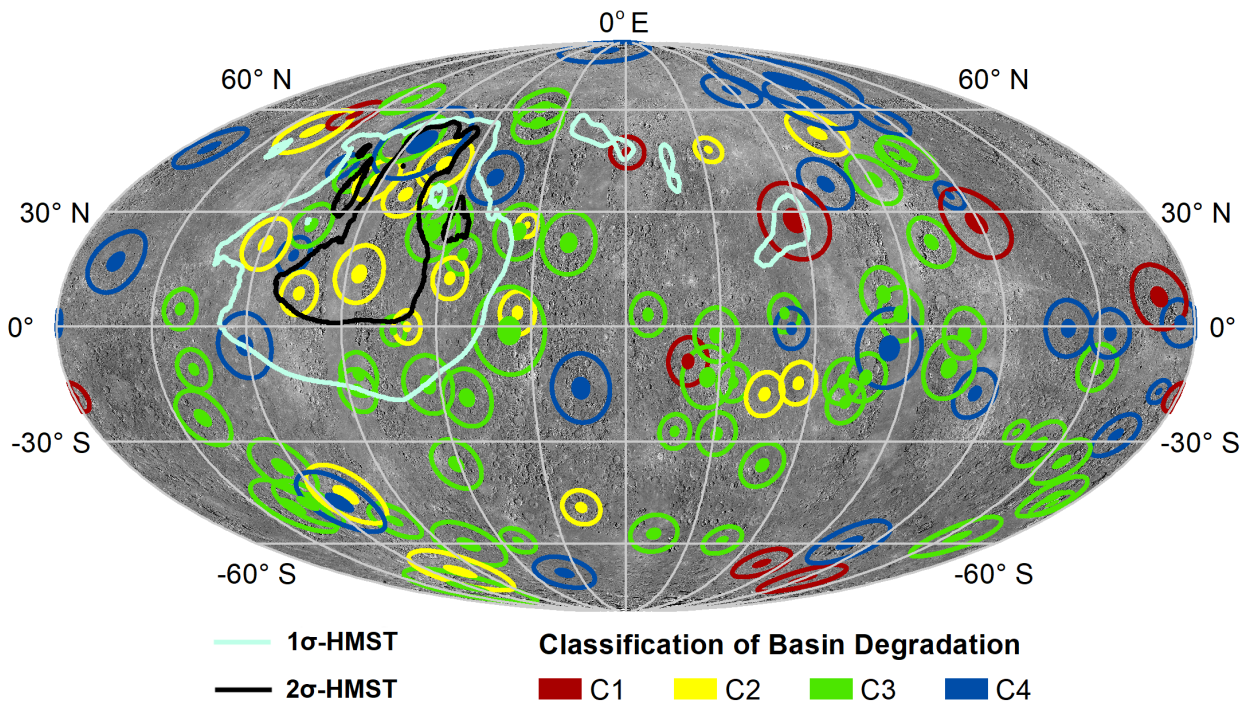
Figure 8. Enhanced colour image of Rachmaninoff Basin (Denevi et al., 2017). The 1σ- and 1.5σ-Mg/Si regions are shown, in gray and black respectively. The DEM contour (Becker et al., 2016) delineates a region 750 m below the geoid, defined by the mean mercurian radius of 2439.4 km.
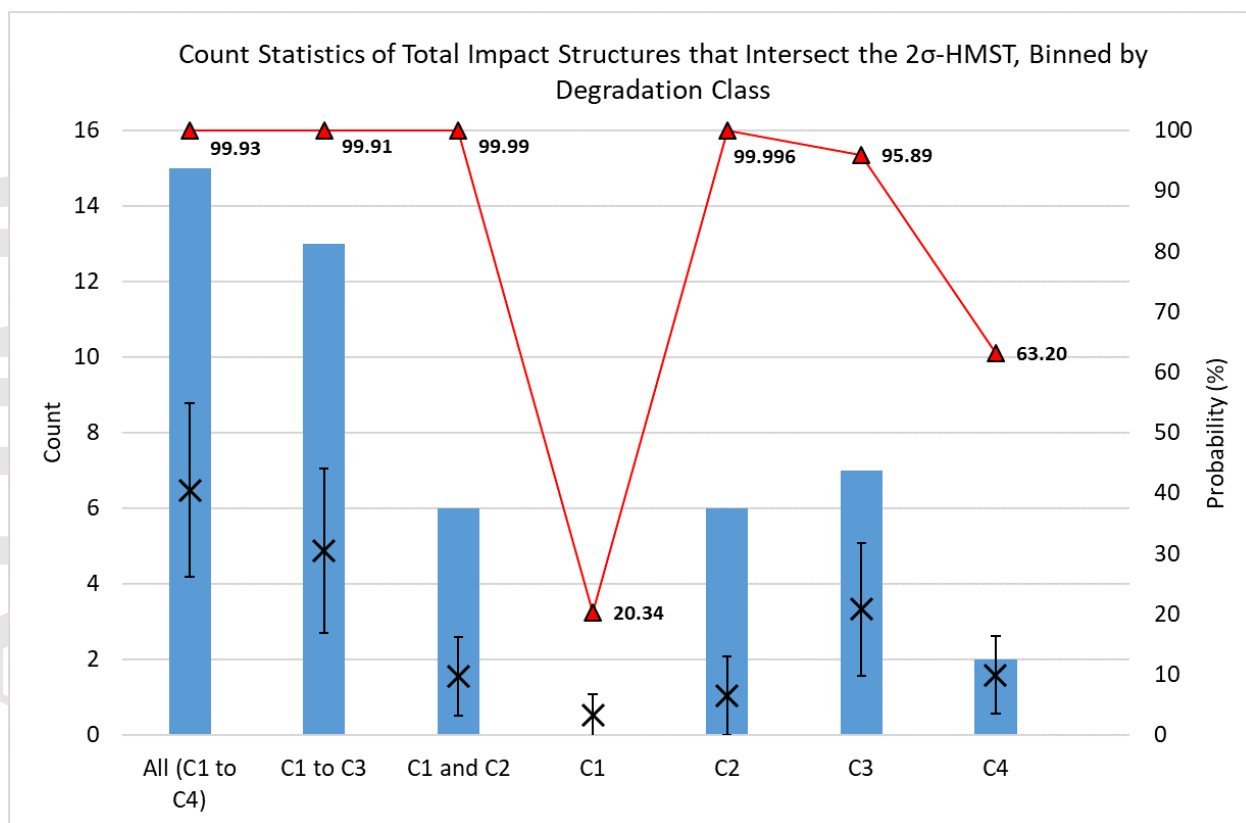
0° E

60°N   60°N
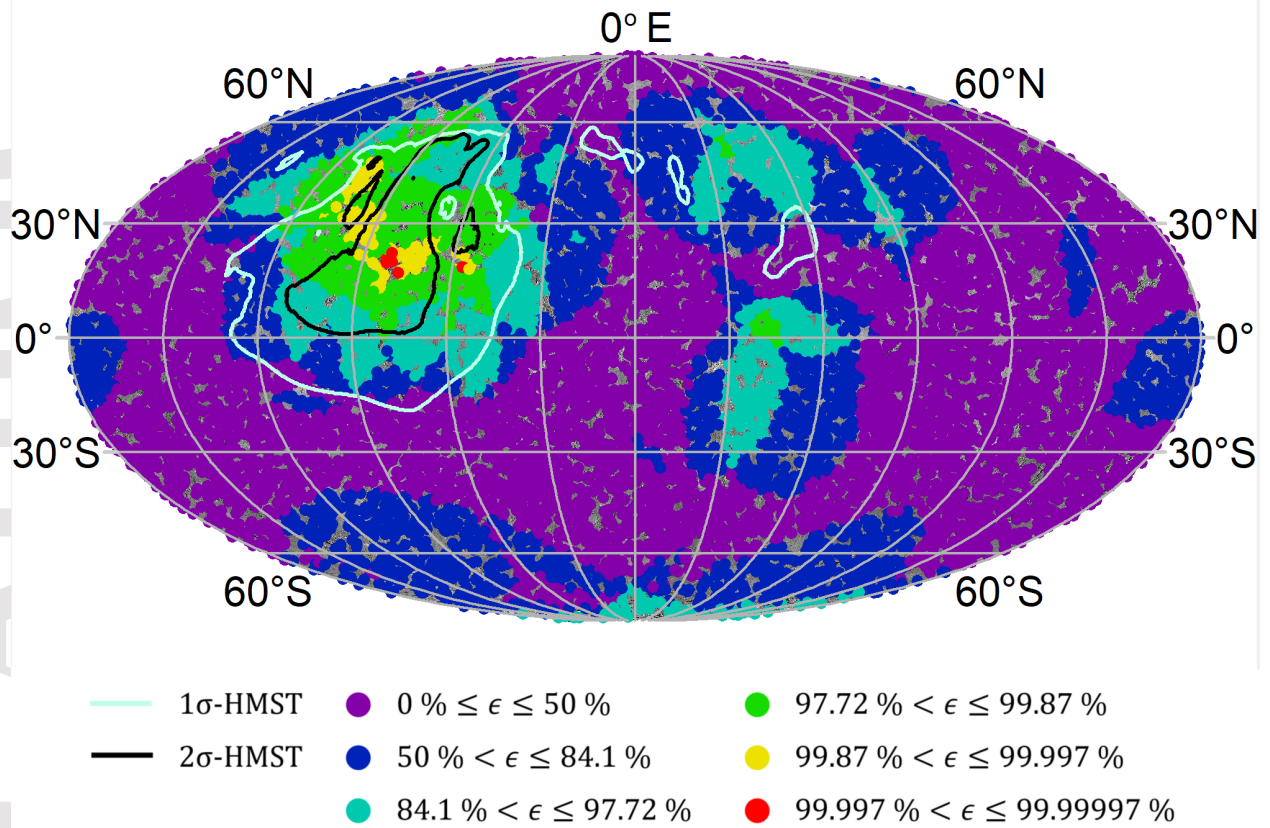
30°N   30°N

0°   0°

30°S   30°S

60°S   60°S

—— 2 sigma Mg/Si contour

—— 1.5 sigma Mg/Si contour

—— 1 sigma Mg/Si contour

Mg/Si (Nittler et al. 2016)

High : 0.782

Low : 0

1σ-HMST

2σ-HMST

Classification of Basin Degradation

C1   C2   C3   C4

Count Statistics of Total Impact Structures that Intersect the 2σ-HMST, Binned by Degradation Class

Depth of Excavation vs Mg/Si for HMT and Similar Basins

Legend:
- Similar PRB
- Similar PRB Mg/Si Mean
- HMT PRB
- HMT PRB Mg/Si Mean
- Planetary Mg/Si Mean
- Planetary Mg/Si STD Margins

Y-axis: Mg/Si
X-axis: Depth of Excavation (km)
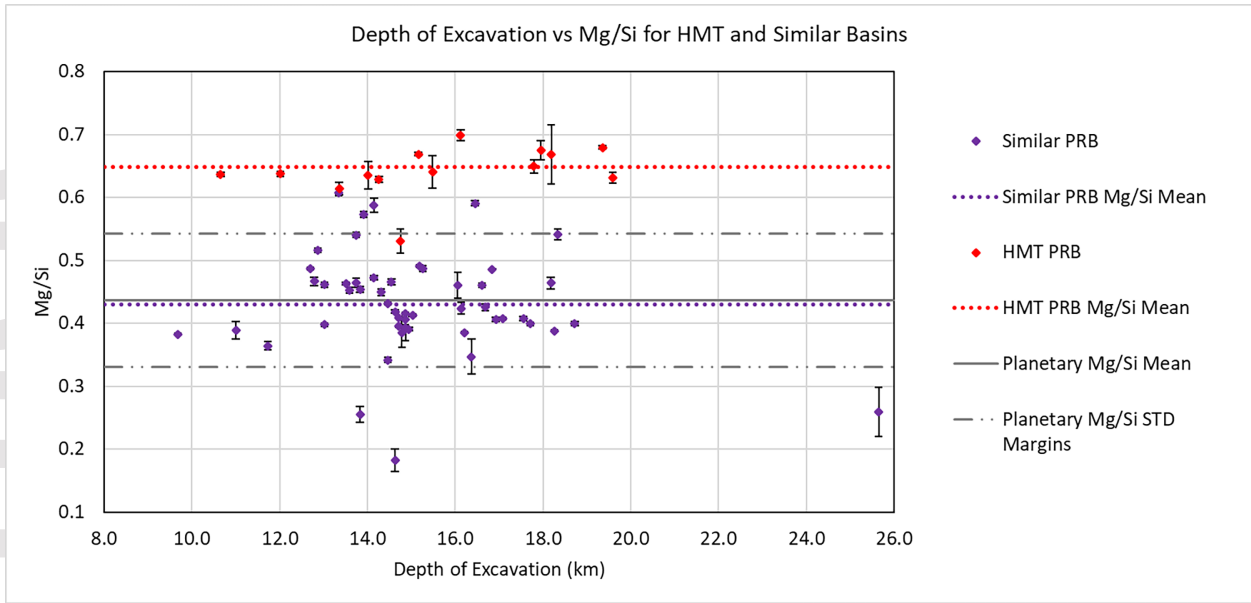
Depth of Excavation and Melting compared to Crustal Thickness for HMT PRB

DEM Contour, minus 750 m
1.5sigma Mg/Si contour
1sigma Mg/Si contour